



THE UNIVERSITY *of* EDINBURGH

Edinburgh Research Explorer

Feed Temperature Effects on Organic Fouling of Reverse Osmosis Membranes: Competition of Interfacial and Transport Properties

Citation for published version:

BinAhmed, S, Hozalski, RM & Romero-Vargas Castrillon, S 2021, 'Feed Temperature Effects on Organic Fouling of Reverse Osmosis Membranes: Competition of Interfacial and Transport Properties', *ACS ES&T Engineering*, vol. 1, no. 3, pp. 591-602. <https://doi.org/10.1021/acsestengg.0c00258>, <https://doi.org/10.1021/acsestengg.0c00258>

Digital Object Identifier (DOI):

<https://doi.org/10.1021/acsestengg.0c00258>
[10.1021/acsestengg.0c00258](https://doi.org/10.1021/acsestengg.0c00258)

Link:

[Link to publication record in Edinburgh Research Explorer](#)

Document Version:

Peer reviewed version

Published In:

ACS ES&T Engineering

General rights

Copyright for the publications made accessible via the Edinburgh Research Explorer is retained by the author(s) and / or other copyright owners and it is a condition of accessing these publications that users recognise and abide by the legal requirements associated with these rights.

Take down policy

The University of Edinburgh has made every reasonable effort to ensure that Edinburgh Research Explorer content complies with UK legislation. If you believe that the public display of this file breaches copyright please contact openaccess@ed.ac.uk providing details, and we will remove access to the work immediately and investigate your claim.



47 **Abstract**

48 We investigated the effect of feed temperature on organic fouling of reverse osmosis (RO)
49 membranes. Experiments were conducted over the range $27 < T < 40$ °C, relevant to feed
50 temperatures in arid, near-equatorial latitudes. Fouling by alginate, a major component of
51 extracellular polymeric substances, was investigated at the nanoscale by means of AFM-based
52 temperature-controlled colloidal-probe force spectroscopy (CPFS). The CPFS results,
53 complemented by interfacial property characterisation (contact angle, surface roughness and
54 charge) conducted under temperature-controlled conditions, enabled us to rationalize the observed
55 fouling kinetics in cross-flow fouling experiments. We observed less severe flux loss at 35 °C (J/J_0
56 = 75%, $t = 24$ hr) compared to 27 °C ($J/J_0 = 65\%$), which is due to weaker adhesion forces with
57 rising temperature. The observed variation in the magnitude of adhesion forces is consistent with
58 the temperature dependence of hydrophobic interactions. At 40 °C, the observed flux loss ($J/J_0 =$
59 68%) was similar to that at 27 °C, despite the fact that adhesion forces are relatively weak (and
60 similar to those at 35 °C). Analysis using a series-resistance model shows that the foulant layer
61 hydraulic resistance is equal at 35 and 40 °C, consistent with the CPFS results. More severe fouling
62 was observed at 40 °C compared to 35 °C, however, due to the higher water permeance at 40 °C,
63 which resulted in a greater flux of foulant to the membrane. Our experiments further show that the
64 fouling layer develops within ~2 hours, during which the flux sharply decreases by 26% at 27 °C,
65 19% at 35 °C, and 22% at 40 °C; thereafter, flux losses are small and temperature independent.
66 CPFS experiments show that this behaviour is due to the foulant layer, which results in weak, often
67 repulsive, and T -independent foulant-foulant interactions, which hinder further foulant deposition.
68 **Keywords:** reverse osmosis, hydrophobic interactions, fouling, wastewater reuse

69 **1. Introduction**

70
71 Population growth and climate change are exerting enormous pressure on the world's water
72 resources.¹⁻³ Over 2.4 billion people inhabit highly water stressed areas (defined as those with a
73 water scarcity index > 0.4), many of which are in densely populated urban agglomerations in which
74 water demand exceeds the watershed capacity.⁴ In addition to increased population, urbanization,
75 and industrialization⁵, climate change is expected to increase water stress through prolonged
76 heatwaves that diminish surface and groundwater supplies.⁶ There is thus an urgent need to tap
77 into unconventional water sources (e.g., brackish water, seawater, and wastewater) to expand the
78 water inventory.^{2,7-9} Water recovered from secondary and tertiary municipal wastewater effluents
79 can supplement water resources¹⁰ through indirect use in agricultural and urban irrigation, cooling
80 towers, and recharge of groundwater aquifers.¹¹ Desalination and advanced wastewater treatment
81 by reverse osmosis (RO) have been instrumental in sustainably extracting potable water from
82 unconventional water sources. Nonetheless, membrane fouling in its various forms (organic,
83 inorganic, colloidal, biological) remains a key obstacle¹²⁻¹⁴, resulting in lower permeability and
84 contaminant rejection^{1,12,14,15}, ultimately increasing energy consumption.¹²

85
86 Research over the past two decades has improved our understanding of the link between fouling
87 propensity and RO membrane interfacial properties. Within the context of organic fouling of
88 polyamide RO membranes, low roughness¹⁶, more hydrophilic^{17,18}, and more negatively charged¹⁹
89 membranes exhibit less pronounced flux losses.¹⁶⁻¹⁹ Studies on the effect of feed water quality
90 have shown that Ca^{2+} causes more severe organic fouling (compared to Mg^{2+} and Na^+) with
91 proteins (bovine serum albumin) and alginate^{20,21}, likely due to calcium-mediated gelation of
92 foulants²¹⁻²³ and Ca^{2+} bridging of carboxyl groups on the membrane and foulant²⁰. Higher ionic
93 strength results in compression of the electrical double layer and shielding of surface charge of

94 both the surface of the membrane and the foulants, resulting in higher fouling rate due to reduced
95 electrostatic repulsion.^{3,20,21} The effect of pH is more pronounced around the isoelectric point (IEP)
96 of the foulant, such that foulant-membrane electrostatic repulsion is reduced and fouling rate
97 increases at a pH equal or less than the IEP of the foulant.^{3,20,24} The presence of organic matter in
98 water contributes to the formation of an organic fouling layer on the surface of the membrane,
99 which can provide nutrients to bacteria and facilitate bacterial adhesion to the surface.^{25–28}
100 Therefore, minimising organic fouling can help delay biofouling by mitigating initial bacterial
101 adhesion to the surface of RO membranes.^{29,30}

102

103 The influence of feed water temperature on membrane performance and fouling has attracted far
104 less attention. Only a few studies have been devoted to this subject^{20,31–33}, despite the increasing
105 use of membrane-based desalination and wastewater reuse in arid, near-equatorial latitudes³⁴
106 where water temperatures can reach 35.5 °C.³⁵ Previous work on the connection between RO
107 membrane transport properties and feed temperature has shown that water permeability^{32,36}
108 increases with increasing temperature, due to lower water viscosity^{37,38} and higher water
109 diffusivity.^{31,32} As a result of increasing temperature, permeate recovery increases^{36,38–40} and
110 energy consumption decreases due to lower pressure requirements.^{39–41} Similarly, the salt
111 permeability coefficient, B_s , is directly proportional to the solute diffusivity, D_s , and partition
112 (solubility) coefficient K_s ,^{31,42,43} both of which increase with temperature, leading to a higher salt
113 flux and lower salt rejection.^{36,39,40,44} In one study, Goosen *et al.*³² observed an increase in permeate
114 flux at a fixed applied pressure as temperature was increased from 20 °C to 40 °C for NaCl
115 concentrations ranging from 0 to 5 % w/v NaCl, suggesting that the membrane undergoes
116 morphological changes such as an increase in the polymer free void volume³². Sharma and

117 Chellam⁴⁵ observed that the network pore size of nanofiltration (NF) membranes increased with
118 increasing temperature (5 – 41 °C). In another study, Goosen *et al.*³³ found that correcting for
119 viscosity changes of water with increasing temperature did not totally account for the increase in
120 water permeance with increasing temperature. The researchers suggested an interplay between
121 feed temperature and applied pressure that affected the membrane void volume. Francis and
122 Pashly³⁸ observed that water recovery and permeate flow increased, while salt rejection decreased,
123 with increasing temperature (20 to 30 °C) when treating seawater (0.5 M NaCl) and brackish water
124 (0.2 M NaCl) with thin-film composite (TFC) RO membranes. Jin *et al.*³¹ attributed the lower
125 rejection of humic acid as total organic carbon (TOC) with increasing temperature ($T = 15$ to 35
126 °C) to increased swelling of the polymer network voids. The rate of fouling was similar at 25 °C
127 and 35 °C while the highest flux decline occurred at 15 °C. The higher applied pressure and the
128 larger size of humic acid aggregates at lower temperatures resulted in a higher resistance of the
129 fouling layer at these temperatures.³¹ On the other hand, Mo *et al.*²⁰ reported an increased rate of
130 protein fouling (50 mg L⁻¹ bovine serum albumin) of RO membranes at higher temperatures (18
131 to 35 °C) and for pH values 4.9, and 7. Baghdadi *et al.*⁴⁶ simulated the performance of two TFC
132 RO membranes with increasing temperature (15 – 45 °C) and observed an increase in salt mass
133 transfer coefficient and a decrease in salt rejection when treating a 35 g L⁻¹ NaCl feed water at a
134 constant hydraulic pressure (800 psi).

135

136 Current investigations of the effect of feed temperature on membrane performance are limited to
137 bench-scale experiments, which describe thermal effects on membrane transport parameters and
138 flux loss, but offer little mechanistic insight.^{20,31–33,46} To explain the connection between feed
139 temperature and the observed fouling kinetics, it is necessary to understand the thermal response

140 of interfacial properties such as membrane hydrophobicity, roughness, and charge. As a step in
141 this direction, we used colloidal probe atomic force microscopy (AFM) measurements to probe
142 the effects of temperature on membrane-foulant and foulant-foulant interactions. We then explored
143 how the temperature dependence of the interfacial properties manifests itself in RO membrane
144 fouling experiments using alginate, a polysaccharide that is abundant in wastewater^{47,48} and in
145 bacterial biofilms^{49,50}, as a model foulant. Our results show that weaker hydrophobic interactions
146 with increasing feed temperature (from 27 to 35 °C) initially decrease membrane fouling, but
147 further increases in feed temperature exacerbate fouling due to an increase in the water permeance
148 of the membrane. Consequently, variation of the feed temperature reveals that fouling is
149 determined by a competition between membrane interfacial and transport properties.

150

151 This paper is structured as follows. In section 2, we describe the experimental protocols for the
152 colloidal-probe AFM and dynamic fouling experiments. We discuss our results in section 3,
153 beginning with the effect of temperature (T) on interfacial properties (section 3.1); the effect of T
154 on foulant-membrane and foulant-foulant interactions, as determined by AFM, is discussed in
155 section 3.2; sections 3.3 and 3.4 present the results of membrane transport and fouling experiments,
156 drawing connections to the interfacial and nanoscale adhesion properties. Concluding remarks are
157 given in section 4.

158

159

160

161

162 **2. Materials and Methods**

163

164 **2.1. Reverse osmosis (RO) membrane.**

165 All experiments were carried out with ESPA2-LD membranes (Hydranautics, Oceanside, CA), a
166 low pressure aromatic polyamide RO membrane commonly employed in wastewater
167 recycling.^{10,51} Membrane coupons ($\sim 15 \times 9 \text{ cm}^2$) were cut out from a 10-cm diameter spiral wound
168 element (membrane area 7.43 m^2), rinsed in ultrapure water (UP) ($18.2 \text{ M}\Omega\text{-cm}$, Barnstead), and
169 stored at $5 \text{ }^\circ\text{C}$ in UP water. The hydraulic resistance and water permeance of the membranes were
170 determined with a UP water feed at $25 \text{ }^\circ\text{C}$. For quality assurance purposes, only membranes with
171 A values within the range specified by the manufacturer ($3.5 - 5.1 \text{ L m}^{-2} \text{ h}^{-1} \text{ bar}^{-1}$) were used for
172 dynamic fouling experiments. Further details on the determination of membrane transport
173 properties are provided in section S.1 of the Supporting Information (SI).

174

175 The hydrophilicity and roughness of ESPA2-LD membranes were characterized at $T = 27, 35,$ and
176 $40 \text{ }^\circ\text{C}$. Hydrophilicity was quantified in terms of water contact angle measurements in a
177 temperature-controlled goniometer (DSA30S, Krüss). Both the temperature-controlled goniometer
178 chamber and liquid dispenser were set to the same temperature, so that the droplet and substrate
179 were in thermal equilibrium throughout the measurement. Root-mean-squared roughness (R_{RMS})
180 was measured in a temperature-controlled fluid cell using an atomic force microscope (MFP-3D-
181 Bio, Asylum Research) in tapping mode. The zeta potential of the membrane was determined from
182 streaming potential measurements using an electrokinetic analyzer (SurPass, Anton Paar).
183 Streaming potential measurements were performed at $27 \text{ }^\circ\text{C}$ and $35 \text{ }^\circ\text{C}$ only ($40 \text{ }^\circ\text{C}$ exceeded the
184 maximum operating temperature of the instrument). Further details on membrane surface
185 characterization are found in section S.2 of the SI.

186

187 **2.2. Organic foulant and feed solution chemistry.**

188 We used alginate, a polysaccharide⁵², as a model foulant representative of extracellular polymeric
189 substances (EPS)⁵³⁻⁵⁶ in secondary wastewater effluent⁵⁵⁻⁵⁷. A 6 g L⁻¹ sodium alginate (SA)
190 (A2033, Millipore Sigma, St Louis, MO) stock solution was prepared in UP water before each
191 dynamic fouling experiment by stirring the solution for 24 hours. Alginate was dosed at a
192 concentration of 250 mg L⁻¹ to a feed solution containing 0.45 mM KH₂PO₄, 0.935 mM NH₄Cl,
193 0.5 mM CaCl₂, 0.5 mM NaHCO₃, 9.20 mM NaCl, and 0.61 mM MgSO₄ at pH 7.4. The inorganic
194 composition of the synthetic wastewater used in all fouling experiments is representative of the
195 inorganic fraction of secondary wastewater effluent from certain wastewater treatment plants in
196 California.^{50,58} The ionic strength of foulant-free synthetic wastewater was 14.7 mM (MinTEQ
197 3.1). The alginate concentration used (250 mg L⁻¹) is much higher than concentrations in real
198 systems (in which TOC concentrations are in the 5-20 mg L⁻¹ range⁵⁹⁻⁶²). An elevated
199 concentration was used to accelerate fouling and ensure fouling can be observed within 24 hours.

200

201 **2.3. Dynamic fouling experiments.**

202 A bench-scale crossflow system (see section S.1) was used for fouling, with each experiment
203 comprising the following stages: 1) Membrane compaction at 500-580 psi with UP water at 25 °C
204 until a steady-state permeate flux was achieved. 2) Stabilization of the permeate flux at $J = 20 \pm 1$
205 L m⁻² h⁻¹ (LMH) for 1 hour at 25 °C to validate the water permeance of the membrane (the
206 manufacturer-specified water permeance for ESPA2-LD membranes is 3.5 – 5.1 LMH bar⁻¹). 3)
207 Adjustment of the temperature of the UP water feed to 27, 35, or 40 °C by means of a heater/chiller
208 (6500 series, Polyscience) followed by overnight stabilization of the permeate flux at $J = 20 \pm 1$

209 LMH (this stage was used to calculate the A at each temperature). 4) Dosing of alginate-free
210 synthetic wastewater into the feed tank, followed by system stabilisation at the desired temperature
211 (27, 35, or 40 °C) at $J = 20 \pm 1$ LMH; this stage typically required stabilisation for 4-6 days, and
212 included sampling of the feed and permeate conductivity to determine conductivity rejection
213 before fouling. 5) Dosing of 250 mg L⁻¹ alginate into the synthetic wastewater feed and initiation
214 of dynamic fouling at an initial flux $J_0 = 20$ L m⁻² h⁻¹; the flux loss during fouling was measured
215 over 24 hours accompanied by sampling of the feed and permeate conductivity and TOC content
216 (2 and 24 hours after initiation of fouling) to calculate conductivity and TOC rejection,
217 respectively. The permeate flow rate was recorded every 0.2 seconds at all phases (except
218 compaction) with a digital flow meter (SLI-2000, Sensirion, Stäfa, Switzerland) and logged to a
219 computer. Further details on the experimental apparatus and fouling experiments can be found in
220 the SI.

221

222 **2.4. Colloidal Probe AFM Force Spectroscopy.**

223

224 *2.4.1. Colloidal probes.*

225 Carboxyl-modified latex (CML) colloidal particles with a nominal diameter of 4 μm were used in
226 all AFM measurements. These polystyrene microspheres have a surface rich in carboxylic acid
227 functional groups^{56,63}, which are commonly found in alginate and other foulants.^{56,64} According to
228 the product specifications (ThermoFisher Scientific, C37253), the CML particles are hydrophobic
229 at low pH and somewhat hydrophilic at high pH. However, other studies have characterized similar
230 CML particles as hydrophobic.⁶⁵ CML particles were received as a 4% w/v suspension in
231 deionized water and were stored at 5 °C until use.

232

233

234 *2.4.2. Preparation of colloidal probes.*

235 The protocol for preparing the colloidal probes was adapted from that reported by others.^{3,63,66} A
236 20- μ L aliquot of CML particle suspension (2500 \times dilution) was deposited on a UV/O₃-cleaned⁶⁷
237 glass slide and dried overnight in a desiccator. An inverted optical microscope (Zeiss Axio
238 Observer A.1) integrated into the AFM was used to guide a tipless AFM cantilever (MLCT-O10
239 cantilever “A”, nominal $k = 0.07$ N/m, Bruker) first towards a small amount of UV-curable glue
240 (Norland 86, Norland optical, Cranbury, NJ) deposited on the glass slide and then towards the
241 CML to be adhered to the cantilever. The prepared AFM colloidal probes were then cured in a
242 solar simulator (Xenon lamp, wavelength > 290 nm, 350 W/m²) for 30 minutes.

243

244 *2.4.3. Experimental conditions.*

245 Measurement of interfacial interactions between the CML probes and the surface of pristine and
246 alginate-fouled ESPA2-LD membranes was performed using an atomic force microscope (MFP-
247 3D-Bio, Asylum Research) equipped with a temperature-controlled fluid cell. Force measurements
248 were conducted at $T = 27$ °C, 35 °C, and 40 °C in two different systems: pristine membranes in
249 20 mg L⁻¹ alginate in synthetic wastewater (a concentration representative of the TOC levels of 5-
250 20 mg L⁻¹^{55,59} in wastewater effluent); and alginate-fouled membranes in synthetic wastewater
251 supplemented with 20 mg L⁻¹ alginate. The former investigates the temperature dependence of
252 foulant-membrane interactions, which determine the initial adhesion of foulant at the early stages
253 of fouling, while the latter measurements investigate foulant-foulant interactions in the subsequent
254 stages, once a foulant layer has formed on the membrane surface.^{3,63,68} Synthetic wastewater

255 supplemented with 20 mg L⁻¹ alginate was freshly prepared prior to each experiment as described
256 in section 2.2. The alginate-fouled membrane substrate was prepared as described in the SI (see
257 section S.1). To distinguish between real CML microsphere adhesion and artifacts resulting from
258 particles contaminated with glue, control measurements were performed using a particle-free
259 cantilever on which we deposited a small amount of cured glue. These measurements (performed
260 in phosphate buffered saline at pH 7.4 on pristine membranes) resulted in distinctly sharp adhesion
261 peaks compared to those of clean CML particles. Probes suspected of glue contamination were
262 discarded. Only data collected with CML particles unaffected by glue artifacts are presented and
263 discussed.

264

265 For individual coupons, force measurements were collected at 27 °C, then 35 °C, and finally at 40
266 °C by ramping up the temperature at a rate of 1 °C/min. After allowing 30 minutes for the
267 cantilever to reach thermal equilibrium, at each set-point temperature the inverse optical lever
268 sensitivity and spring constant were determined (the latter according to the thermal noise
269 method⁶⁹). Measurements at the three temperatures were repeated in triplicate (i.e., with three
270 different membrane coupons) with three independently functionalized AFM cantilevers. A total of
271 ≥ 105 force curves were collected at each temperature. To account for membrane surface
272 heterogeneity⁷⁰, adhesion forces were measured at each temperature over at least 11 randomly
273 selected spots (collecting 3 force curves per spot) located at least 6 μm apart from one another.
274 The AFM probe was checked at the end of every experiment to verify that the CML particle was
275 not dislocated and that it had remained at its original position during force measurements.

276

277 Force curves were recorded at 200 nm/s approach-retraction speed, a cycle speed that results in
278 negligible dissipative friction on the CML particle.⁷¹ The CML probe engaged the membrane
279 substrate with a trigger force (F_{trigger} ; defined in Figure S3 of the SI) of 2 nN, while remaining in
280 contact with the surface of the pristine or fouled membrane for a dwell time of 5 seconds. A
281 constant force was maintained between the CML particle and membrane surface during the dwell
282 time by setting the feedback channel to deflection. AFM experiments were performed in open loop
283 to minimize noise in the collected forces. The choice of trigger force was based on calculations of
284 the permeation drag force exerted on a 4- μm diameter particle experiencing a flux of 20 LMH,
285 typical of RO operation (see section S.3). For data analysis, the minimum measurable force – 30
286 pN – was determined by measuring the noise in the free end of several force curves at each
287 temperature. Parameters collected from force curves are identified in Figure S3. From the
288 extension force curve: snap-in force (F_{snap}) is defined as the adhesion force observed as the
289 colloidal probe approaches the membrane substrate,^{72–74} snap-in separation (R_{snap}) is identified as
290 the distance at which the snap-in event occurs.^{75,76} From the retraction force curve: peak adhesion
291 force (F_{peak}) is defined as the maximum adhesion force observed as the colloidal probe is pulled
292 away from the membrane; rupture separation (R) is the distance at which interactions between the
293 probe and the membrane surface vanish.⁷⁷

294

295 **2.5. Statistical analysis.**

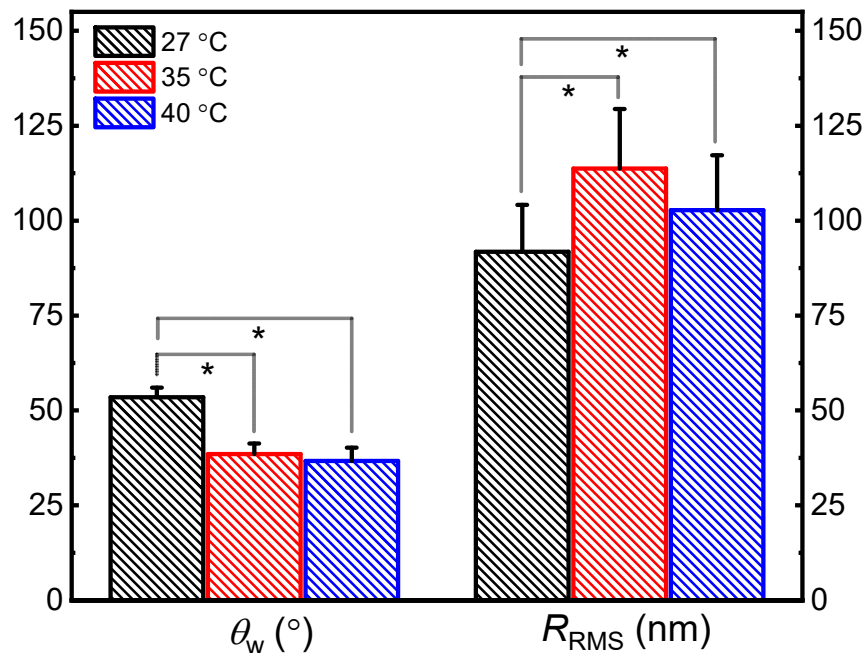
296 Unpaired two-sided homoscedastic (equal variance) t -tests were used to determine statistical
297 significance of the results.

298 **3. Results and Discussion**

299

300 **3.1. Characterization of RO membrane.**

301 The contact angle of sessile water droplets (θ_w) reflects membrane hydrophilicity⁷⁸⁻⁸⁰ and depends
302 on membrane properties (surface roughness, surface charge, and surface functional groups)^{78,80-82}
303 as well as on external conditions such as water temperature^{78,83} and salt concentration^{78,84}. The
304 effect of temperature on θ_w and root-mean-squared roughness (R_{RMS}) of pristine RO membranes
305 is shown in Figure 1. The measured θ_w at 27 °C ($53.5 \pm 2.5^\circ$) is similar to that reported by other
306 studies (43° - 55°)^{10,85} on ESPA2 membranes at room temperature. The contact angle at 27 °C was
307 significantly higher than that at 35 °C ($38.5 \pm 2.8^\circ$; $p < 0.01$) and at 40 °C ($36.7 \pm 3.5^\circ$; $p < 0.01$)
308 but θ_w at 35 °C and 40 °C were similar ($p = 0.078$). The decrease in contact angle with increasing
309 temperature is a manifestation of a general surface phenomenon: as first postulated by Zisman⁸⁶
310 and Petke and Ray⁸⁷, θ_w decreases with rising T for common liquids whose surface tension
311 decreases with increasing T . It is expected that the membrane would swell more at higher
312 temperatures, as has been observed with polyamide membranes^{31,88}, due to the increasing
313 wettability of the membrane by water. Consistent with this expectation, we observed (Figure 1) an
314 increase in R_{RMS} of the pristine RO membrane with increasing temperature (representative AFM
315 scans at each T are given in Figure S1). R_{RMS} increased from 91.8 ± 12.3 nm at 27 °C to $113.7 \pm$
316 15.7 nm at 35 °C ($p < 0.01$) and 102.8 ± 14.5 nm at 40 °C ($p < 0.05$), while the R_{RMS} values at 35
317 °C and 40 °C were similar ($p = 0.0562$).



319

320 **Figure 1:** Sessile water drop contact angle (θ_w) and root-mean-squared roughness (R_{RMS}) measurements of
 321 pristine ESPA2-LD membranes at $T = 27, 35,$ and 40 °C (* denotes a significant difference between the
 322 indicated samples, $p < 0.05$).

323 The zeta potential (ζ) of ESPA2-LD membranes at 27 °C (Figure S2) varied from -7 mV to -35
 324 mV as pH was increased from 4 to 10 with $\zeta \approx -30$ mV at pH = 7.4. The negative charge of
 325 polyamide is due to the deprotonation of carboxylic acid groups on the membrane surface⁸⁴, and
 326 presumably to the adsorption of hydroxide ions on uncharged hydrophobic regions on polyamide.
 327 Hydroxide ion adsorption is posited as the cause of the negative charge of many hydrophobic
 328 surfaces.^{89,90} At 27 °C and 35 °C we observe similar charging behavior at pH < 7 , while a less
 329 negative ζ is observed at basic pH at 35 °C. We ascribe this behavior to a lower extent of adsorption
 330 of hydroxide ions resulting from the decreasing hydrophobicity of the interface at 35 °C (cf. Figure
 331 1).

332

333 **3.2. Effect of temperature on adhesion forces.**

334 In this section, we investigate the T dependence of membrane surface forces using AFM-based
335 force spectroscopy measurements with a carboxylated colloidal probe (a mimic of alginate). We
336 considered pristine membranes as well as alginate-fouled membranes (prepared as explained in
337 the SI) to investigate the T dependence of foulant-membrane and foulant-foulant interactions.
338 Previous work has used AFM to relate foulant-membrane interactions to the rate of fouling, finding
339 a strong correlation between fouling propensity and the strength of adhesion forces determined by
340 AFM.^{56,63} On the other hand, the effect of temperature, investigated below, has hitherto been
341 overlooked. We analyzed both the approach and retraction segments of the force curves. The
342 approach segment provides information about the mechanism of adhesion of foulant molecules as
343 they first encounter the membrane interface, i.e., whether foulants experience repulsive or
344 attractive forces during initial adhesion (and the strength of such interactions). The retraction
345 segment quantifies the force necessary to detach adhered foulants.

346

347 Before discussing the force spectroscopy data quantitatively (Figures 2-3, S6-S9), a few qualitative
348 features of the force curves are noteworthy. Figures S3 and S4 show representative force-distance
349 curves, including the approach segment as the inset, collected over pristine and alginate-fouled
350 membranes, respectively. The CML microsphere experiences a small repulsive force ($F_{\text{rep}} \sim 43\text{-}50$
351 pN, see Figure S3) as it approaches the surface of pristine membranes; this repulsion is likely steric
352 as it is observed at separations (8 – 9 nm) greater than the Debye length (2.5 nm at $I = 14.7$ mM).
353 At shorter separations, the polystyrene chains on the microsphere surface eventually encounter the
354 surface, and the microsphere experiences a sudden attractive force known as a ‘snap-in’ or ‘jump-
355 to-contact’ spring instability^{91,92}: at the snap-in point, the gradient of the particle-membrane force

356 exceeds the cantilever spring constant, the cantilever becomes unstable (i.e., the particle-surface
357 force and the cantilever elastic force are no longer in balance), and jump-to-contact occurs. This
358 jump-to-contact force has been attributed to the van der Waals attractive force between the tip and
359 the surface.⁷²⁻⁷⁴ The snap-in force is not observed in the approach force curves recorded over
360 alginate-fouled membranes (inset in Figure S4(a), (b)); instead, the force is repulsive throughout
361 the contact region, but the gradual increase in the loading force is consistent with compression of
362 the soft alginate layer by the colloidal microsphere.⁷⁶ The retraction force curves over pristine
363 membranes display sharp (often multiple) adhesion peaks (Figure S3), presumed to be due to the
364 stretching of polystyrene chains upon probe pull-off. In some cases, we observe tethering events
365 (Figure S5 (a), (b)), which are likely due to detachment of alginate molecules bridging (with the
366 aid of Ca^{2+}) the CML probe and the membrane surface⁹³, or desorption⁹⁴ of alginate molecules
367 from the membrane. Over alginate-fouled membranes, we observe adhesion peaks, likely due to
368 alginate desorption (Figure S4(a)). In addition, a fraction of the force curves (quantified below)
369 are repulsive during retraction (Figure S4(b)) indicating that the alginate layer prevented the
370 adhesion events that are otherwise observed in pristine membranes.

371
372 Next, we discuss quantitatively the force spectroscopy data in terms of the distribution of peak
373 adhesion, snap-in forces, and rupture separations (defined in Section 2.4.3 and in Figure S3). The
374 data are plotted as histograms in Figures 2-3 and S6-S9. The distribution of snap-in forces (F_{snap})
375 and snap-in separations (R_{snap}) on pristine membranes is shown in Figures S6 and S7. As shown in
376 Figure S6(d), the attraction is strongest at 27 °C when the membrane is least hydrophilic and
377 smoothest (see Figure 1), with an average snap-in force (\bar{F}_{snap}) of 115 pN compared to 81 pN at
378 35 °C ($p = 0.039$) and 92 pN at 40 °C ($p = 0.138$). The force curves that do not display a snap-in

379 force (i.e., purely repulsive approach curves tallied as the “NO” column in Figures S6(a-c)),
380 representing between 31.4% and 45.7% of the forces were assigned $F_{\text{snap}} = 0$ when calculating the
381 average in Figure S6(d). A similar trend – decreasing \bar{F}_{snap} with rising T – is observed when the
382 average excluded the non-adhesive approaches, Figure S6(e). The probability with which snap-in
383 events occurred (ranging between 54.3% and 68.6%), and the distance at which snap-in is
384 established (R_{snap} , Figure S7), ~8-9 nm on average, showed no discernible T dependence.

385

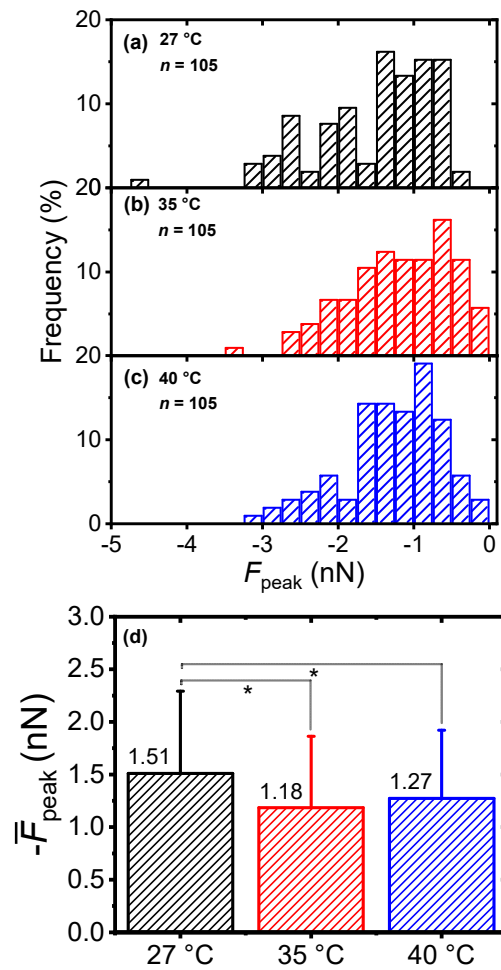
386 Figure 2(a-c) shows the peak adhesion force (F_{peak}) distribution (defined in Figure S3) of CML
387 probes collected over pristine membranes at $T = 27, 35,$ and 40 °C. The distribution of F_{peak} at 27
388 °C shows more frequent strong adhesion events ($-3 \text{ nN} < F_{\text{peak}} < -2 \text{ nN}$) compared to higher
389 temperatures. Moreover, Figure 2(d) shows that the average adhesion force at 27 °C ($\bar{F}_{\text{peak}} = -1.51$
390 $\pm 0.78 \text{ nN}$) is stronger than that at 35 °C ($\bar{F}_{\text{peak}} = -1.18 \pm 0.68 \text{ nN}$; $p = 0.0015$) and 40 °C ($\bar{F}_{\text{peak}} =$
391 $-1.27 \pm 0.65 \text{ nN}$; $p = 0.0174$). Adhesion forces at 35 °C and 40 °C were similar ($p = 0.339$), which
392 is consistent with the invariant contact angle and surface roughness at these same temperatures (cf.
393 Figure 1). We expect adhesion forces to decrease at $T > 40$ °C, as observed by other studies.^{95,96}
394 Such a range, however, is not environmentally relevant, and was therefore not studied in our work.
395 On the other hand, the distribution of rupture separations (R) over pristine membranes (Figure S8),
396 ranging between 120 and 150 nm, was not dependent on T .

397

398 The decreasing adhesion force with increasing temperature observed during approach (F_{snap} ;
399 Figure S6) and retraction (F_{peak} ; Figure 2) followed the same trend with T as hydrophobic
400 interactions, suggesting that the T dependence of organic foulant adhesion shows close
401 resemblance to hydrophobic hydration phenomena. Weakening of hydrophobic adhesion forces

402 with rising T agree with previous force spectroscopic experiments.^{95,96} The decreasing magnitude
403 of adhesion forces is also consistent with theoretical investigations showing that macroscopic
404 surfaces become less hydrophobic with rising T .⁹⁷ As first envisaged by Stillinger⁹⁸, hydration of
405 large hydrophobes requires the formation of a water-depleted interface around the solute, akin to
406 a liquid-vapor interface. Building on these ideas, Chandler and co-workers showed that the free
407 energy of hydrophobic solvation scales with the liquid-vapor surface tension of water (γ) as $\Delta G \sim$
408 $4\pi\gamma R^2$ (where R is the hydrophobic solute radius)⁹⁹. Accordingly, the temperature dependence of
409 ΔG approaches that of γ (i.e., decreases with rising temperature), with hydrophobic hydration
410 becoming more energetically favorable at higher T .⁹⁷

411
412 While hydrophobic interactions appear to be the main driving force of foulant-membrane adhesion,
413 we cannot rule out the possibility that adhesion is aided by Ca^{2+} -mediated^{13,63} bridging interactions
414 between the deprotonated carboxylic groups on the CML particle and the surface of the membrane.
415 Both the membrane (Figure S2) and alginate are negatively charged at $\text{pH} > 6$ because most of the
416 carboxylic groups are deprotonated⁹³ ($\text{pK}_a = 3.5 - 4.7$ ^{3,16,100}). The presence of deprotonated
417 carboxylic acid groups is suggested by the negative charge of both the membrane (Figure S2) and
418 alginate.^{16,93}

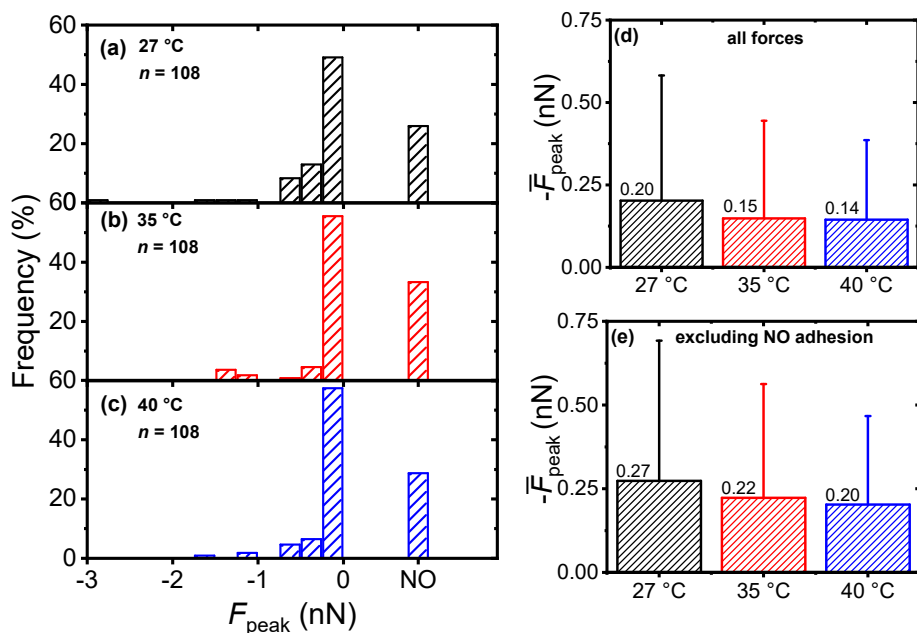


420
 421 **Figure 2:** (a-c) Distribution of peak adhesion forces (F_{peak}) of CML colloidal probes on pristine ESPA2-
 422 LD membranes for each indicated temperature (given in the inset along with the number of force
 423 measurements, n). (d) Average peak adhesion force (\bar{F}_{peak}) at each temperature calculated from (a-c) (*
 424 denotes statistical significance with $p < 0.05$). Error bars denote one standard deviation. Data were collected
 425 in synthetic wastewater supplemented with 20 mg L⁻¹ sodium alginate ($t_{\text{contact}} = 5$ s; $F_{\text{trigger}} = 2$ nN; pH 7.4;
 426 $I = 14.7$ mM).

427
 428 Substantially different surface forces dominate the interactions between the colloidal particle and
 429 the alginate-fouled membrane. These results are presented in Figure 3(a-c) for $T = 27, 35,$ and 40
 430 °C, respectively. As mentioned previously, snap-in events are absent in measurements with fouled
 431 membranes; we observe instead repulsive forces during approach at any temperature (see Figure
 432 S4). Repulsive forces are also observed in 25.9-33.3% of retraction force curves (denoted by the
 433 “NO” column in Figure 3 (a-c)). These repulsive forces can be attributed to strong electrostatic

434 repulsion between the CML particle and the more negative membrane surface in the presence of
435 alginate fouling layer.¹⁰¹ Wang *et al.*⁶⁸ also attributed weaker alginate-alginate adhesion forces to
436 electrostatic repulsive forces resulting from the more negative charge of alginate compared to other
437 foulants (bovine serum albumin and effluent organic matter). In contrast to the pristine membrane,
438 the average peak adhesion force (\bar{F}_{peak}) over fouled membranes is significantly weaker in
439 magnitude and less sensitive to temperature ($p > 0.05$ for all pairwise comparisons) irrespective
440 of whether repulsive forces curves are included in the average (Figure 3(d)) or not (Figure 3(e)).

441
442 The distribution of rupture separations (R) of CML particles over fouled membranes at $T = 27, 35,$
443 and $40\text{ }^{\circ}\text{C}$ is shown in Figure S9. Although \bar{R} is similar for all the temperatures investigated ($p >$
444 0.05 for all pairwise comparisons), \bar{R} has a larger value ($\approx 0.6\text{ }\mu\text{m}$) on the fouled membranes than
445 on pristine membranes (compare Figure S9 with Figure S8). Longer rupture separations are likely
446 due to desorption of alginate molecules from the membrane surface during probe retraction.



447

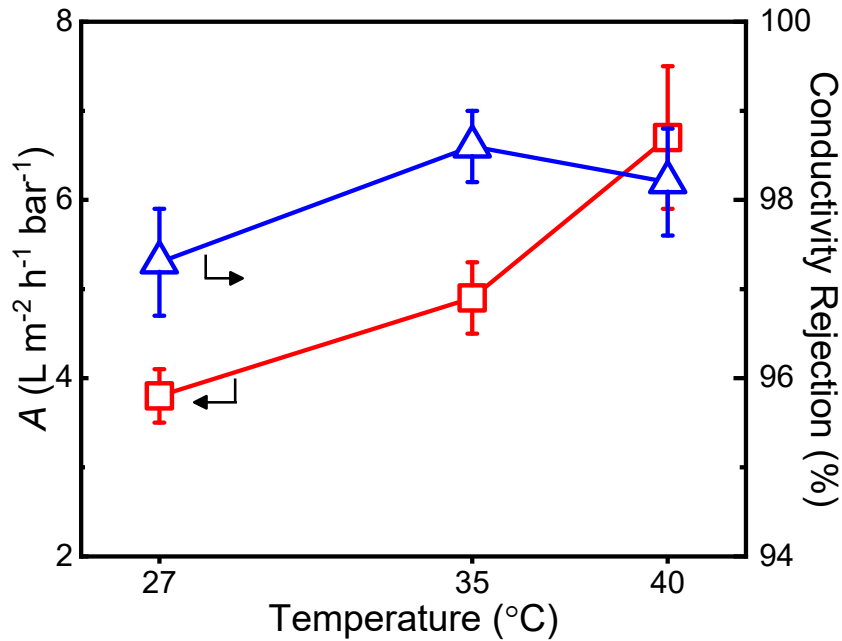
448 **Figure 3:** (a-c) Distribution of peak adhesion forces (F_{peak}) of CML colloidal probes on alginate-fouled
 449 ESPA2-LD membranes for each indicated temperature (given in the inset along with the number of force
 450 measurements, n). Force curves in which $|F_{\text{peak}}| < 30$ pN are tallied as the “NO” column (30 pN is the
 451 magnitude of the noise observed in the free end of force curves). (d) Average peak adhesion force (\bar{F}_{peak})
 452 at each temperature calculated from (a-c) including the non-adhesive events as $\bar{F}_{\text{peak}} = 0$. (e) Average peak
 453 adhesion force (\bar{F}_{peak}) at each temperature calculated from (a-c) excluding the non-adhesive events. Error
 454 bars denote one standard deviation. Data were collected in synthetic wastewater supplemented with 20 mg
 455 L^{-1} sodium alginate ($t_{\text{contact}} = 5$ s; $F_{\text{trigger}} = 2$ nN; pH 7.4; $I = 14.7$ mM).

456

457 3.3. Effect of temperature on membrane transport parameters.

458 Having established the T -dependence of membrane adhesive properties, we next examine the
 459 impact of T on transport and selectivity during membrane filtration. The effect of temperature on
 460 the membrane permeance to water and conductivity rejection of ESPA2-LD thin-film composite
 461 membranes is shown in Figure 4.

462



463 **Figure 4:** Effect of temperature on the permeance to water (A) and conductivity rejection (right y-axis) of
 464 ESPA2-LD membranes at $T = 27, 35,$ and 40 °C. The error bars denote one standard deviation. Alginate-
 465 free synthetic wastewater feed was used to determine conductivity rejection (number of measurements $n =$
 466 6 at 27 °C, $n = 6$ at 35 °C, and $n = 8$ at 40 °C). All data determined at a permeate flux $J = 20 \pm 1$ LMH.
 467

468 In agreement with previous experiments (5 °C $< T < 60$ °C)^{32,39,102}, A increases with feed
 469 temperature (Figure 4) from 3.8 ± 0.3 LMH bar⁻¹ at 27 °C to 4.9 ± 0.4 and 6.7 ± 0.8 LMH bar⁻¹ at
 470 35 °C and 40 °C, respectively. The change in permeance with temperature is due to the dependence
 471 of A on water viscosity and diffusivity^{31,39}: $A \propto \frac{D_{w,m}}{T}$ ($D_{w,m}$ is the water diffusivity in the
 472 membrane) and $D_{w,m} \propto \frac{T}{\mu}$ (μ is the dynamic water viscosity).³¹ As a result, A will be inversely
 473 proportional to μ which, in turn, varies inversely with temperature.^{36,102,103} Another possible factor
 474 contributing to the increase in A is the thermal expansion of the polyamide network³¹: the increase
 475 in surface roughness with T (Figure 1) is presumably due to thermal expansion of the polyamide
 476 active layer.³¹ In addition, the increase in roughness observed between 27 °C and 35 °C (Figure 1)
 477 – resulting in a larger effective permeable area¹⁰⁴ – may also be responsible for the increase in A ¹⁰⁵
 478 observed between 27 °C and 35 °C.

479

480 Conductivity rejection was found to be weakly dependent on T , ranging from $97.3 \pm 0.6\%$ at 27
481 °C to $98.6 \pm 0.4\%$ and $98.2 \pm 0.6\%$ at 35 °C and 40 °C, respectively. While these observations are
482 at odds with the expected temperature dependence of the solute diffusivity, D_s , and solubility, K_s ,
483 in the membrane (both D_s and K_s increase with increasing temperature)^{31,39,106}, the results in Figure
484 4 appear to be in agreement with other studies showing negligible temperature dependence of the
485 reflection coefficient over a similar temperature range.³²

486

487

488 **3.4. Effect of temperature on organic fouling.**

489

490 The effect of temperature on alginate fouling is investigated in Figure 5(a), showing the normalized
491 permeate flux, J/J_0 as a function of time. The time dependence of the permeate flux exhibits
492 common features at all temperatures, indicative of a transition of fouling dominated by foulant-
493 membrane interactions to a regime determined by foulant-foulant interactions.¹⁰⁷ A steep flux loss
494 (26% at 27 °C, 19% at 35 °C, and 22% at 40 °C) within the first two hours is followed by slow flux
495 decline at longer times (Figure 5(a)). This behavior is consistent with our colloidal AFM data: at
496 short time scales, fouling is dominated by strong foulant-clean membrane interactions (Figures 2
497 and S6), leading to the rapid formation of a foulant layer and significant flux loss. At longer times
498 scales ($t \gtrsim 2$ h), weakly adhesive or repulsive foulant-foulant interactions (Figure 3) cause J/J_0 to
499 decrease at a much slower rate. On the other hand, the extent of flux loss is different at each
500 temperature. Fouling is most severe at 27 °C, with a flux loss of 35% after 24 h compared to 25%
501 at 35 °C and 32% at 40 °C. The more significant fouling at 27 °C is consistent with the stronger
502 hydrophobic interactions at this temperature (cf. Figure 2). However, at 35 and 40 °C different

503 fouling propensity does not reflect the similar adhesion forces observed in Figure 2. Thus,
504 interfacial behavior alone does not explain the observed fouling behavior.

505

506 To reconcile the fouling experiments in Figure 5(a) with the interfacial behavior presented in
507 Figure 2, we quantified the resistance contributed by the foulant layer to water transport using a
508 resistance-in-series model.^{108,109} Within this approach, the overall transport resistance of the fouled
509 membrane is given by the sum of the individual hydraulic resistances of the polyamide (A^{-1}) and a
510 (time-dependent) hydraulic resistance due to the foulant layer, $A_f(t)^{-1}$. The resulting expression for
511 the time-dependent flux through the fouled membrane is,

512

$$513 \quad J(t) = \frac{1}{A^{-1} + A_f(t)^{-1}} (\Delta p - \Delta \pi) \quad (1)$$

514 where $\Delta \pi$ is the osmotic pressure difference between the feed and the permeate. Dividing Equation
515 (1) by the steady-state water flux through the clean membrane ($J_o = A(\Delta p - \Delta \pi)$) yields,

516

$$517 \quad \frac{J(t)}{J_o} = \frac{1}{1 + \frac{A}{A_f(t)}} = \frac{1}{1 + R_f(t)A} \quad (2)$$

518

519 where the inverse of the permeability of the foulant layer is expressed as a hydraulic resistance,
520 $R_f(t) = A_f(t)^{-1}$. Equation (1) shows that two mechanisms could contribute to flux loss: fouling, which
521 increases $R_f(t)$ as the foulant layer develops; and increasing water permeance (e.g., due to T), which
522 will also lower J/J_o due to the increased convective flux of foulant to the membrane. Based on the
523 characterization results, we speculate that the smaller flux loss at 35 °C compared to 27 °C is
524 primarily due to the effect of the interfacial properties on the foulant layer: a lower R_f value at 35

525 °C results from a thinner foulant layer due to a more hydrophilic membrane (Figure 1) and weaker
526 hydrophobic interactions (Figure 2) at 35 °C versus 27 °C. The smaller R_f mitigates the effect of a
527 larger value of A at 35 °C compared to 27 °C (Figure 4), with the net effect being a smaller flux
528 loss at 35 °C. Conversely, raising T from 35 to 40 °C brings about a negligible change in interfacial
529 properties and R_f (similar hydrophilicity and adhesion forces, cf. Figures 1 and 2), but a significant
530 increase in A (Figure 4) that results in more severe flux loss at 40 °C compared to 35 °C.

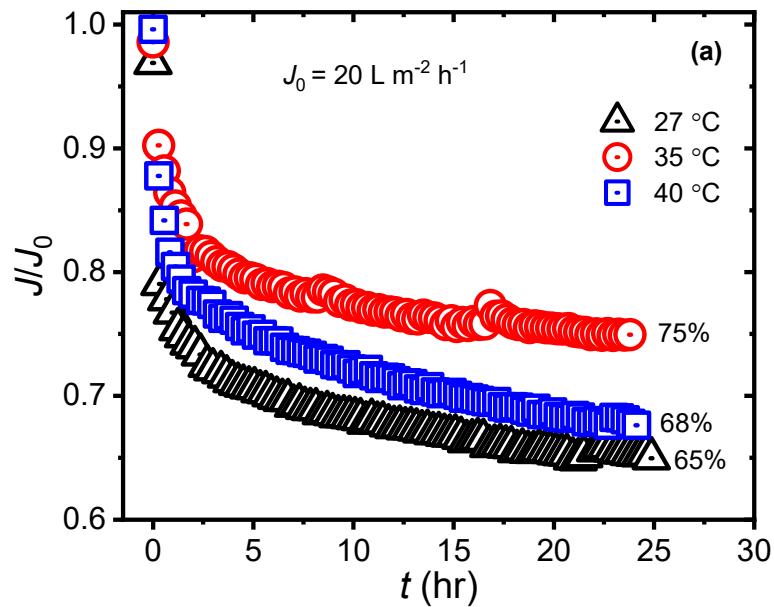
531

532 These arguments are supported by the experimental data. Solving for R_f using Equation (2) with
533 data from Figures 4 and 5 ($A_{35\text{ °C}} = 4.9 \text{ LMH bar}^{-1}$, $A_{40\text{ °C}} = 6.7 \text{ LMH bar}^{-1}$, $(J(t = 24 \text{ h})/J_0)_{35\text{ °C}} =$
534 0.75 and $(J(t = 24 \text{ h})/J_0)_{40\text{ °C}} = 0.68$) yields $R_{f, 35\text{ °C}} = 0.07 \text{ bar LMH}^{-1} = R_{f, 40\text{ °C}}$, i.e., similar foulant
535 layer resistances consistent with the AFM results (Figure 2); thus, the greater flux loss at 40 °C
536 compared to 35 °C stems from $A_{40\text{ °C}} > A_{35\text{ °C}}$ (Figure 4). On the other hand, $R_{f, 27\text{ °C}} = 0.14 \text{ bar}$
537 LMH^{-1} , a significantly higher resistance (due to stronger adhesion at 27 °C) that causes a more
538 pronounced flux loss compared to experiments at higher T . As we elaborate in section S.4 (SI), we
539 estimate the thickness of the foulant layer at $O(10 \text{ }\mu\text{m})$, and the fraction of foulant adhered to the
540 membrane at ca. 3% of the total mass of alginate. Thus, we can neglect the contribution to the
541 slow-down of the fouling rate resulting from a lower concentration of alginate in the feed.

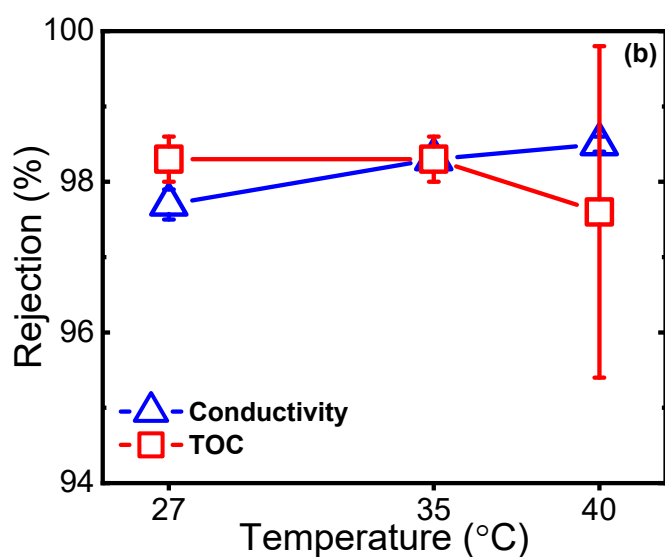
542

543 Finally, the results of conductivity and TOC rejection at each temperature are summarized in
544 Figure 5(b). These data are derived from measurements at $t = 2 \text{ h}$ and 24 h after initiation of the
545 fouling experiment and are reported as a single average as they were similar (within 1%) to one
546 another at each temperature. Conductivity rejection remained approximately constant with
547 increasing temperature, exhibiting values similar to those of the clean membrane (see Figure 4).

548 Similarly, TOC rejection shown in Figure 5(b) is independent of temperature. Although increased
549 passage of dissolved alginate could be expected with rising temperature on account of membrane
550 swelling³¹, the high TOC rejection suggests that alginate (likely found as Ca⁺²-complexed
551 aggregates) are large enough (> 1 nm¹¹⁰, compared to sub-nanometer voids in polyamide^{1,105}) as
552 to deposit on the surface of the membrane as a fouling layer. The TOC passage observed (1.7-
553 2.4%) is likely due to low molecular weight impurities in alginate (e.g., polyphenols and
554 proteins¹¹¹). Similar TOC passage has been observed by previous studies with humic acid.³¹



555



556 **Figure 5:** Effect of temperature on the performance of ESPA2-LD membranes during alginate fouling: (a)
 557 flux decline of ESPA2-LD membranes over 24 hours during accelerated fouling with 250 mg L⁻¹ sodium
 558 alginate for each indicated feed temperature given in the inset. Due to the noise underlying the permeate
 559 flow rate measurements, flux data was smoothed using a locally estimated scatterplot smoothing algorithm
 560 (loess) implemented in Origin 2018 (Northampton, MA). (b) Average conductivity and TOC rejection after
 561 initiation of fouling. Error bars denote one standard deviation. Experimental conditions: initial permeate
 562 flux $J_0 = 20$ LMH; feed solution 14.7 mM synthetic wastewater at pH = 7.4 supplemented with 250 mg L⁻¹
 563 sodium alginate; crossflow velocity = 15.8 cm/s.
 564

565

566 4. Conclusion

567 We have shown that membrane interfacial and transport properties play competing roles during
 568 alginate fouling of reverse osmosis membranes at different temperatures. Colloidal probe force
 569 spectroscopy (CPFS) measurements show that foulant-membrane interactions are markedly
 570 temperature-dependent (Figure 2). Rising temperature *weakens* foulant adhesion, given that
 571 foulant-membrane hydrophobic interactions, which become weaker with increasing temperature,
 572 drive adhesion onto clean membranes. Conversely, the monotonic increase in water permeance
 573 with temperature (Figure 4) worsens fouling, which suggests that lower operating pressures (and
 574 hence lower fluxes) will be needed during extreme temperature conditions (e.g., heat waves) to
 575 avoid exposing the membrane to excessive fouling. Interestingly, our results suggest that

576 membrane hydrophilicity, a key interfacial property in membrane development, becomes less
577 relevant at high feed temperatures, since membranes become *ipso facto* less hydrophobic at higher
578 temperatures (Figure 1 and 2). CPFS measurements further show that the alginate layer is self-
579 limiting: once an adlayer of a critical thickness is formed, deposition of additional foulant
580 molecules is hindered by weak (or repulsive) foulant-foulant interactions (Figure 3), which appear
581 to be temperature independent. Our results also suggest possible lines for future inquiry.
582 Understanding of the process conditions that lead to the formation of the critical foulant layer is
583 crucial for effective fouling management. Given the preeminent role of hydrophobic interactions
584 in alginate fouling, experiments at lower temperature (which strengthen foulant-membrane
585 hydrophobic interactions) should be conducted to understand fouling under feed conditions
586 relevant to temperate and cold climates. These experiments would also be useful in the formulation
587 of cleaning-in-place formulations tailored to specific feed temperatures.

588 **Acknowledgements**

589 This work was supported by grants to S.R.-V.C. from 3M Co. (Non-Tenured Faculty Award), and
590 the Environment and Natural Resources Trust Fund, as recommended by the Legislative-Citizen
591 Commission on Minnesota Resources. We thank Hydranautics (Oceanside, CA) for supplying the
592 membranes used in the initial stages of this investigation. The technical assistance of Wieslaw J.
593 Suszynski (Coating Process Fundamentals Visualization Laboratory, University of Minnesota)
594 with contact angle measurements is gratefully acknowledged. S. B.-A. acknowledges support from
595 the Graduate School at the University of Minnesota through a Doctoral Dissertation Fellowship.

596

597

598

599 **Supporting Information**

600 The Supporting Information is available free of charge on the ACS Publications website at
601 <http://pubs.acs.org>.

- 602 • Additional materials and methods (sections S.1 and S.2). Calculation of the
603 permeate drag force exerted on a colloidal particle (section S.3). Estimation of the
604 foulant layer thickness and adsorbed mass (section S.4). Tapping-mode AFM
605 images of polyamide membranes at various temperatures (Figure S1). ζ -Potential
606 of polyamide membranes at various temperature and pH conditions (Figure S2).
607 Representative force curves over pristine and alginate-fouled membranes (Figures
608 S3-S5). Snap-in forces (Figure S6) and snap-in distances (Figure S7) on pristine
609 membranes. Rupture separations over pristine (Figure S8) and alginate-fouled
610 (Figure S9) membranes.

611
612 **References**

- 613 (1) Werber, J. R.; Osuji, C. O.; Elimelech, M. Materials for Next-Generation Desalination and
614 Water Purification Membranes. *Nat. Rev. Mater.* **2016**, 1–15.
615 <https://doi.org/10.1038/natrevmats.2016.18>.
- 616 (2) Jjemba, P. K.; Weinrich, L. A.; Cheng, W.; Giraldo, E.; LeChevallier, M. W. Regrowth of
617 Potential Opportunistic Pathogens and Algae in Reclaimed-Water Distribution Systems.
618 *Appl. Environ. Microbiol.* **2010**, 76 (13), 4169–4178. [https://doi.org/10.1128/AEM.03147-](https://doi.org/10.1128/AEM.03147-09)
619 09.
- 620 (3) Ang, W. S.; Elimelech, M. Protein (BSA) Fouling of Reverse Osmosis Membranes:
621 Implications for Wastewater Reclamation. *J. Memb. Sci.* **2007**, 296 (1–2), 83–92.
622 <https://doi.org/10.1016/j.memsci.2007.03.018>.
- 623 (4) Oki, T.; Kanae, S. Global Hydrological Cycles and World Water Resources. *Science (80-*
624 *).* **2006**, 313 (5790), 1068–1072. <https://doi.org/10.1126/science.1128845>.
- 625 (5) Gullinkala, T.; Escobar, I. C. Membranes for Water Treatment Applications – An
626 Overview. In *ACS Symposium Series*; 2011; pp 155–170. [https://doi.org/10.1021/bk-2011-](https://doi.org/10.1021/bk-2011-1078.ch010)
627 1078.ch010.
- 628 (6) Kelley, C. P.; Mohtadi, S.; Cane, M. A.; Seager, R.; Kushnir, Y. Climate Change in the
629 Fertile Crescent and Implications of the Recent Syrian Drought. *Proc. Natl. Acad. Sci.*
630 **2015**, 112 (11), 3241–3246. <https://doi.org/10.1073/pnas.1421533112>.
- 631 (7) Alvarez, P. J. J.; Chan, C. K.; Elimelech, M.; Halas, N. J.; Villagrán, D. Emerging
632 Opportunities for Nanotechnology to Enhance Water Security. *Nat. Nanotechnol.* **2018**, 13
633 (8), 634–641. <https://doi.org/10.1038/s41565-018-0203-2>.
- 634 (8) Elimelech, M.; Phillip, W. A. The Future of Seawater Desalination: Energy, Technology,
635 and the Environment. *Science (80-.).* **2011**, 333 (6043), 712–717.
636 <https://doi.org/10.1126/science.1200488>.
- 637 (9) Jarusutthirak, C.; Amy, G. Membrane Filtration of Wastewater Effluents for Reuse:
638 Effluent Organic Matter Rejection and Fouling. *Water Sci. Technol.* **2001**, 43 (10), 225–
639 232.
- 640 (10) Fujioka, T.; Khan, S. J.; McDonald, J. A.; Henderson, R. K.; Poussade, Y.; Drewes, J. E.;
641 Nghiem, L. D. Effects of Membrane Fouling on N-Nitrosamine Rejection by
642 Nanofiltration and Reverse Osmosis Membranes. *J. Memb. Sci.* **2013**, 427, 311–319.
643 <https://doi.org/10.1016/j.memsci.2012.09.055>.

- 644 (11) Petala, M.; Tsiridis, V.; Samaras, P.; Zouboulis, A.; Sakellariopoulos, G. P. Wastewater
645 Reclamation by Advanced Treatment of Secondary Effluents. *Desalination* **2006**, *195*,
646 109–118.
- 647 (12) Doederer, K.; Farré, M. J.; Pidou, M.; Weinberg, H. S.; Gernjak, W. Rejection of
648 Disinfection By-Products by RO and NF Membranes: Influence of Solute Properties and
649 Operational Parameters. *J. Memb. Sci.* **2014**, *467*, 195–205.
650 <https://doi.org/10.1016/j.memsci.2014.05.029>.
- 651 (13) Wu, J.; Contreras, A. E.; Li, Q. Studying the Impact of RO Membrane Surface Functional
652 Groups on Alginate Fouling in Seawater Desalination. *J. Memb. Sci.* **2014**, *458*, 120–127.
653 <https://doi.org/10.1016/j.memsci.2014.01.056>.
- 654 (14) Kang, G.; Cao, Y. Development of Antifouling Reverse Osmosis Membranes for Water
655 Treatment: A Review. *Water Res.* **2012**, *46* (3), 584–600.
656 <https://doi.org/10.1016/j.watres.2011.11.041>.
- 657 (15) Varin, K. J.; Lin, N. H.; Cohen, Y. Biofouling and Cleaning Effectiveness of Surface
658 Nanostructured Reverse Osmosis Membranes. *J. Memb. Sci.* **2013**, *446*, 472–481.
659 <https://doi.org/10.1016/j.memsci.2013.06.064>.
- 660 (16) Li, Q.; Xu, Z.; Pinnau, I. Fouling of Reverse Osmosis Membranes by Biopolymers in
661 Wastewater Secondary Effluent: Role of Membrane Surface Properties and Initial
662 Permeate Flux. *J. Memb. Sci.* **2007**, *290* (1–2), 173–181.
663 <https://doi.org/10.1016/j.memsci.2006.12.027>.
- 664 (17) Xu, P.; Drewes, J. E.; Kim, T.-U.; Bellona, C.; Amy, G. Effect of Membrane Fouling on
665 Transport of Organic Contaminants in NF/RO Membrane Applications. *J. Memb. Sci.*
666 **2006**, *279* (1–2), 165–175. <https://doi.org/10.1016/j.memsci.2005.12.001>.
- 667 (18) Zou, L.; Vidalis, I.; Steele, D.; Michelmore, A.; Low, S. P.; Verberk, J. Q. J. C. Surface
668 Hydrophilic Modification of RO Membranes by Plasma Polymerization for Low Organic
669 Fouling. *J. Memb. Sci.* **2011**, *369* (1–2), 420–428.
670 <https://doi.org/10.1016/j.memsci.2010.12.023>.
- 671 (19) Ghanbari, M.; Emadzadeh, D.; Lau, W. J.; Matsuura, T.; Ismail, A. F. Synthesis and
672 Characterization of Novel Thin Film Nanocomposite Reverse Osmosis Membranes with
673 Improved Organic Fouling Properties for Water Desalination. *RSC Adv.* **2015**, *5* (27),
674 21268–21276. <https://doi.org/10.1039/c4ra16177g>.
- 675 (20) Mo, H.; Tay, K. G.; Ng, H. Y.; Guan Tay, K.; Yong Ng, H. Fouling of Reverse Osmosis
676 Membrane by Protein (BSA): Effects of PH, Calcium, Magnesium, Ionic Strength and
677 Temperature. *J. Memb. Sci.* **2008**, *315*, 28–35.
678 <https://doi.org/10.1016/j.memsci.2008.02.002>.
- 679 (21) Lee, S.; Ang, W. S.; Elimelech, M. Fouling of Reverse Osmosis Membranes by
680 Hydrophilic Organic Matter: Implications for Water Reuse. *Desalination* **2006**, *187*, 313–
681 321.
- 682 (22) Ang, W. S.; Lee, S.; Elimelech, M. Chemical and Physical Aspects of Cleaning of
683 Organic-Fouled Reverse Osmosis Membranes. *J. Memb. Sci.* **2006**, *272* (1–2), 198–210.
684 <https://doi.org/10.1016/j.memsci.2005.07.035>.
- 685 (23) Katsoufidou, K.; Yiantsios, S. G.; Karabelas, A. J. An Experimental Study of UF
686 Membrane Fouling by Humic Acid and Sodium Alginate Solutions: The Effect of
687 Backwashing on Flux Recovery. *Desalination* **2008**, *220* (1–3), 214–227.
688 <https://doi.org/10.1016/j.desal.2007.02.038>.
- 689 (24) Jones, K. L.; O'Neil, C. R. Ultrafiltration of Protein and Humic Substances: Effect

- 690 of Solution Chemistry on Fouling and Flux Decline. *J. Memb. Sci.* **2001**, *193* (2), 163–
691 173. [https://doi.org/10.1016/S0376-7388\(01\)00492-6](https://doi.org/10.1016/S0376-7388(01)00492-6).
- 692 (25) Bazaka, K.; Jacob, M. V.; Crawford, R. J.; Ivanova, E. P. Efficient Surface Modification
693 of Biomaterial to Prevent Biofilm Formation and the Attachment of Microorganisms.
694 *Appl. Microbiol. Biotechnol.* **2012**, *95* (2), 299–311. [https://doi.org/10.1007/s00253-012-](https://doi.org/10.1007/s00253-012-4144-7)
695 4144-7.
- 696 (26) Friedlander, R. S.; Vogel, N.; Aizenberg, J. Role of Flagella in Adhesion of *Escherichia*
697 *Coli* to Abiotic Surfaces. *Langmuir* **2015**, *31* (22), 6137–6144.
698 <https://doi.org/10.1021/acs.langmuir.5b00815>.
- 699 (27) Garrett, T. R.; Bhakoo, M.; Zhang, Z. Bacterial Adhesion and Biofilms on Surfaces. *Prog.*
700 *Nat. Sci.* **2008**, *18* (9), 1049–1056. <https://doi.org/10.1016/j.pnsc.2008.04.001>.
- 701 (28) Araújo, E. A.; de Andrade, N. J.; da Silva, L. H. M.; de Carvalho, A. F.; de Silva, C. A. S.;
702 Ramos, A. M. Control of Microbial Adhesion as a Strategy for Food and Bioprocess
703 Technology. *Food Bioprocess Technol.* **2010**, *3* (3), 321–332.
704 <https://doi.org/10.1007/s11947-009-0290-z>.
- 705 (29) Baek, Y.; Yu, J.; Kim, S.-H.; Lee, S.; Yoon, J. Effect of Surface Properties of Reverse
706 Osmosis Membranes on Biofouling Occurrence under Filtration Conditions. *J. Memb. Sci.*
707 **2011**, *382* (1–2), 91–99. <https://doi.org/10.1016/j.memsci.2011.07.049>.
- 708 (30) Suwarno, S. R.; Hanada, S.; Chong, T. H.; Goto, S.; Henmi, M.; Fane, A. G. The Effect of
709 Different Surface Conditioning Layers on Bacterial Adhesion on Reverse Osmosis
710 Membranes. *Desalination* **2016**, *387*, 1–13. <https://doi.org/10.1016/j.desal.2016.02.029>.
- 711 (31) Jin, X.; Jawor, A.; Kim, S.; Hoek, E. M. V. V. Effects of Feed Water Temperature on
712 Separation Performance and Organic Fouling of Brackish Water RO Membranes.
713 *Desalination* **2009**, *239* (1–3), 346–359. <https://doi.org/10.1016/j.desal.2008.03.026>.
- 714 (32) Goosen, M. F. A.; Sablani, S. S.; Al-Maskari, S. S.; Al-Belushi, R. H.; Wilf, M. Effect of
715 Feed Temperature on Permeate Flux and Mass Transfer Coefficient in Spiral-Wound
716 Reverse Osmosis Systems. *Desalination* **2002**, *144* (1–3), 367–372.
717 [https://doi.org/10.1016/S0011-9164\(02\)00345-4](https://doi.org/10.1016/S0011-9164(02)00345-4).
- 718 (33) Goosen, M. F. A. A.; Sablani, S.; Cin, M. D.; Wilf, M. Effect of Cyclic Changes in
719 Temperature and Pressure on Permeation Properties of Composite Polyamide Seawater
720 Reverse Osmosis Membranes. *Sep. Sci. Technol.* **2010**, *46* (1), 14–26.
721 <https://doi.org/10.1080/01496395.2010.502552>.
- 722 (34) Kim, S.; Lee, S.; Lee, E.; Sarper, S.; Kim, C. H.; Cho, J. Enhanced or Reduced
723 Concentration Polarization by Membrane Fouling in Seawater Reverse Osmosis (SWRO)
724 Processes. *Desalination* **2009**, *247* (1–3), 162–168.
725 <https://doi.org/10.1016/j.desal.2008.12.021>.
- 726 (35) John, V. C.; Coles, S. L.; Abozed, A. I. Seasonal Cycles of Temperature, Salinity and
727 Water Masses of the Western Arabian Gulf. *Oceanol. Acta* **1990**, *13* (3), 273–282.
- 728 (36) Agashichev, S. P.; Lootah, K. N. Influence of Temperature and Permeate Recovery on
729 Energy Consumption of a Reverse Osmosis System. *Desalination* **2003**, *154* (3), 253–266.
730 [https://doi.org/10.1016/S0011-9164\(03\)80041-3](https://doi.org/10.1016/S0011-9164(03)80041-3).
- 731 (37) Schaep, J.; Van Der Bruggen, B.; Uytterhoeven, S.; Croux, R.; Vandecasteele, C.; Wilms,
732 D.; Van Houtte, E.; Vanlerberghe, F. Removal of Hardness from Groundwater by
733 Nanofiltration. *Desalination* **1998**, *119* (1–3), 295–301. [https://doi.org/10.1016/S0011-](https://doi.org/10.1016/S0011-9164(98)00172-6)
734 9164(98)00172-6.
- 735 (38) Francis, M. J. J.; Pashley, R. M. M. The Effects of Feed Water Temperature and

- 736 Dissolved Gases on Permeate Flow Rate and Permeate Conductivity in a Pilot Scale
737 Reverse Osmosis Desalination Unit. *Desalin. Water Treat.* **2011**, *36* (1–3), 363–373.
738 <https://doi.org/10.5004/dwt.2011.2511>.
- 739 (39) Jawor, A.; Hoek, E. M. V. Effects of Feed Water Temperature on Inorganic Fouling of
740 Brackish Water RO Membranes. *Desalination* **2009**, *235* (1–3), 44–57.
741 <https://doi.org/10.1016/j.desal.2008.07.004>.
- 742 (40) Al-Mutaz, I. S.; Al-Ghunaimi, M. A. Performance of Reverse Osmosis Units at High
743 Temperatures. In *IDA World Congress on Desalination and Water Reuse*; 2001.
- 744 (41) Wilf, M.; Bartels, C. Optimization of Seawater RO Systems Design. *Desalination* **2005**,
745 *173* (1), 1–12. <https://doi.org/10.1016/j.desal.2004.06.206>.
- 746 (42) Geise, G. M.; Park, H. B.; Sagle, A. C.; Freeman, B. D.; McGrath, J. E. Water
747 Permeability and Water/Salt Selectivity Tradeoff in Polymers for Desalination. *J. Memb.*
748 *Sci.* **2011**, *369* (1–2), 130–138. <https://doi.org/10.1016/j.memsci.2010.11.054>.
- 749 (43) Geise, G. M.; Paul, D. R.; Freeman, B. D. Fundamental Water and Salt Transport
750 Properties of Polymeric Materials. *Progress in Polymer Science.* 2014, pp 1–24.
751 <https://doi.org/10.1016/j.progpolymsci.2013.07.001>.
- 752 (44) Ormanci-Acar, T.; Celebi, F.; Keskin, B.; Mutlu-Salmanlı, O.; Agtas, M.; Turken, T.;
753 Tufani, A.; Imer, D. Y.; Ince, G. O.; Demir, T. U.; et al. Fabrication and Characterization
754 of Temperature and PH Resistant Thin Film Nanocomposite Membranes Embedded with
755 Halloysite Nanotubes for Dye Rejection. *Desalination* **2018**, *429*, 20–32.
756 <https://doi.org/10.1016/j.desal.2017.12.005>.
- 757 (45) Sharma, R. R.; Chellam, S. Temperature Effects on the Morphology of Porous Thin Film
758 Composite Nanofiltration Membranes. *Environ. Sci. Technol.* **2005**, *39* (13), 5022–5030.
759 <https://doi.org/10.1021/es0501363>.
- 760 (46) Baghdadi, Y. N.; Alnouri, S. Y.; Matsuura, T.; Tarboush, B. J. A. Temperature Effects on
761 Concentration Polarization Thickness in Thin-Film Composite Reverse Osmosis
762 Membranes. *Chem. Eng. Technol.* **2018**, *41* (10), 1905–1912.
763 <https://doi.org/10.1002/ceat.201800184>.
- 764 (47) Listiarini, K.; Chun, W.; Sun, D. D.; Leckie, J. O. Fouling Mechanism and Resistance
765 Analyses of Systems Containing Sodium Alginate, Calcium, Alum and Their Combination
766 in Dead-End Fouling of Nanofiltration Membranes. *J. Memb. Sci.* **2009**, *344* (1–2), 244–
767 251. <https://doi.org/10.1016/j.memsci.2009.08.010>.
- 768 (48) Romero-Vargas Castrillón, S.; Lu, X.; Shaffer, D. L.; Elimelech, M. Amine Enrichment
769 and Poly(Ethylene Glycol) (PEG) Surface Modification of Thin-Film Composite Forward
770 Osmosis Membranes for Organic Fouling Control. *J. Memb. Sci.* **2014**, *450*, 331–339.
771 <https://doi.org/10.1016/j.memsci.2013.09.028>.
- 772 (49) Boyd, A.; Chakrabarty, A. M. Pseudomonas Aeruginosa Biofilms: Role of the Alginate
773 Exopolysaccharide. *J. Ind. Microbiol.* **1995**, *15* (3), 162–168.
- 774 (50) Herzberg, M.; Elimelech, M. Biofouling of Reverse Osmosis Membranes: Role of
775 Biofilm-Enhanced Osmotic Pressure. *J. Memb. Sci.* **2007**, *295* (1–2), 11–20.
776 <https://doi.org/10.1016/j.memsci.2007.02.024>.
- 777 (51) Bellona, C.; Heil, D.; Yu, C.; Fu, P.; Drewes, J. E. The Pros and Cons of Using
778 Nanofiltration in Lieu of Reverse Osmosis for Indirect Potable Reuse Applications. *Sep.*
779 *Purif. Technol.* **2012**, *85*, 69–76. <https://doi.org/10.1016/j.seppur.2011.09.046>.
- 780 (52) Ci, S. X.; Huynh, T. H.; Louie, L. W.; Yang, A.; Beals, B. J.; Ron, N.; Tsang, W.-G.;
781 Soon-Shiong, P.; Desai, N. P. Molecular Mass Distribution of Sodium Alginate by High-

- 782 Performance Size-Exclusion Chromatography. *J. Chromatogr. A* **1999**, *864* (2), 199–210.
783 [https://doi.org/10.1016/S0021-9673\(99\)01029-8](https://doi.org/10.1016/S0021-9673(99)01029-8).
- 784 (53) Ye, Y.; Le Clech, P.; Chen, V.; Fane, A. G.; Jefferson, B. Fouling Mechanisms of
785 Alginate Solutions as Model Extracellular Polymeric Substances. *Desalination* **2005**, *175*
786 (1), 7–20. <https://doi.org/10.1016/j.desal.2004.09.019>.
- 787 (54) Matin, A.; Shafi, H.; Wang, M.; Khan, Z.; Gleason, K.; Rahman, F. Reverse Osmosis
788 Membranes Surface-Modified Using an Initiated Chemical Vapor Deposition Technique
789 Show Resistance to Alginate Fouling under Cross-Flow Conditions: Filtration &
790 Subsequent Characterization. *Desalination* **2016**, *379*, 108–117.
791 <https://doi.org/10.1016/j.desal.2015.11.003>.
- 792 (55) Katsoufidou, K.; Yiantsios, S. G.; Karabelas, A. J. Experimental Study of Ultrafiltration
793 Membrane Fouling by Sodium Alginate and Flux Recovery by Backwashing. *J. Memb.*
794 *Sci.* **2007**, *300* (1–2), 137–146. <https://doi.org/10.1016/j.memsci.2007.05.017>.
- 795 (56) Lu, X.; Romero-Vargas Castrillón, S.; Shaffer, D. L.; Ma, J.; Elimelech, M. In Situ
796 Surface Chemical Modification of Thin-Film Composite Forward Osmosis Membranes
797 for Enhanced Organic Fouling Resistance. *Environ. Sci. Technol.* **2013**, *47* (21).
798 <https://doi.org/10.1021/es403179m>.
- 799 (57) Ang, W. S.; Yip, N. Y.; Tiraferri, A.; Elimelech, M. Chemical Cleaning of RO
800 Membranes Fouled by Wastewater Effluent: Achieving Higher Efficiency with Dual-Step
801 Cleaning. *J. Memb. Sci.* **2011**, *382* (1–2), 100–106.
802 <https://doi.org/10.1016/j.memsci.2011.07.047>.
- 803 (58) Tiraferri, A.; Kang, Y.; Giannelis, E. P.; Elimelech, M. Superhydrophilic Thin-Film
804 Composite Forward Osmosis Membranes for Organic Fouling Control: Fouling Behavior
805 and Antifouling Mechanisms. *Environ. Sci. Technol.* **2012**, *46* (20), 11135–11144.
806 <https://doi.org/10.1021/es3028617>.
- 807 (59) Bartels, C. R.; Wilf, M.; Andes, K.; Iong, J. Design Considerations for Wastewater
808 Treatment by Reverse Osmosis. *Water Sci. Technol.* **2005**, *51* (6–7), 473–482.
809 <https://doi.org/10.2166/wst.2005.0670>.
- 810 (60) Khan, M. T.; Busch, M.; Molina, V. G.; Emwas, A.-H.; Aubry, C.; Croue, J.-P. How
811 Different Is the Composition of the Fouling Layer of Wastewater Reuse and Seawater
812 Desalination RO Membranes? *Water Res.* **2014**, *59*, 271–282.
813 <https://doi.org/10.1016/j.watres.2014.04.020>.
- 814 (61) Kim, H.-C.; Dempsey, B. A. Comparison of Two Fractionation Strategies for
815 Characterization of Wastewater Effluent Organic Matter and Diagnosis of Membrane
816 Fouling. *Water Res.* **2012**, *46* (11), 3714–3722.
817 <https://doi.org/https://doi.org/10.1016/j.watres.2012.04.025>.
- 818 (62) Michael-Kordatou, I.; Michael, C.; Duan, X.; He, X.; Dionysiou, D. D.; Mills, M. A.;
819 Fatta-Kassinos, D. Dissolved Effluent Organic Matter: Characteristics and Potential
820 Implications in Wastewater Treatment and Reuse Applications. *Water Res.* **2015**, *77*, 213–
821 248. <https://doi.org/10.1016/j.watres.2015.03.011>.
- 822 (63) Li, Q.; Elimelech, M. Organic Fouling and Chemical Cleaning of Nanofiltration
823 Membranes: Measurements and Mechanisms. *Environ. Sci. Technol.* **2004**, *38* (17), 4683–
824 4693. <https://doi.org/10.1021/es0354162>.
- 825 (64) Mi, B.; Elimelech, M. Organic Fouling of Forward Osmosis Membranes: Fouling
826 Reversibility and Cleaning without Chemical Reagents. *J. Memb. Sci.* **2010**, *348* (1–2),
827 337–345. <https://doi.org/10.1016/j.memsci.2009.11.021>.

- 828 (65) Behrens, S. H.; Christl, D. I.; Emmerzael, R.; Schurtenberger, P.; Borkovec, M. Charging
829 and Aggregation Properties of Carboxyl Latex Particles: Experiments versus DLVO
830 Theory. *Langmuir* **2000**, *16* (6), 2566–2575. <https://doi.org/10.1021/la991154z>.
- 831 (66) Beaussart, A.; El-Kirat-Chatel, S.; Sullan, R. M. A.; Alsteens, D.; Herman, P.; Derclaye,
832 S.; Dufrêne, Y. F. Quantifying the Forces Guiding Microbial Cell Adhesion Using Single-
833 Cell Force Spectroscopy. *Nat. Protoc.* **2014**, *9* (5), 1049–1055.
834 <https://doi.org/10.1038/nprot.2014.066>.
- 835 (67) Zhang, X. H.; Quinn, A.; Ducker, W. A. Nanobubbles at the Interface between Water and
836 a Hydrophobic Solid. *Langmuir* **2008**, *24* (9), 4756–4764.
837 <https://doi.org/10.1021/la703475q>.
- 838 (68) Wang, L.; Miao, R.; Wang, X.; Lv, Y.; Meng, X.; Yang, Y.; Huang, D.; Feng, L.; Liu, Z.;
839 Ju, K. Fouling Behavior of Typical Organic Foulants in Polyvinylidene Fluoride
840 Ultrafiltration Membranes: Characterization from Microforces. *Environ. Sci. Technol.*
841 **2013**, *47* (8), 3708–3714. <https://doi.org/10.1021/es4004119>.
- 842 (69) Hutter, J. L.; Bechhoefer, J. Calibration of Atomic-Force Microscope Tips. *Rev. Sci.*
843 *Instrum.* **1993**, *64* (7), 1868–1873. <https://doi.org/10.1063/1.1143970>.
- 844 (70) Allen, A.; Semião, A. J. C.; Habimana, O.; Heffernan, R.; Safari, A.; Casey, E.
845 Nanofiltration and Reverse Osmosis Surface Topographical Heterogeneities: Do They
846 Matter for Initial Bacterial Adhesion? *J. Memb. Sci.* **2015**, *486*, 10–20.
847 <https://doi.org/10.1016/j.memsci.2015.03.029>.
- 848 (71) Lo, Y.-S.; Simons, J.; Beebe, T. P. Temperature Dependence of the Biotin-Avidin Bond-
849 Rupture Force Studied by Atomic Force Microscopy. *J. Phys. Chem. B* **2002**, *106* (38),
850 9847–9852. <https://doi.org/10.1021/jp020863+>.
- 851 (72) Heinz, W. F.; Hoh, J. H. Getting Physical with Your Chemistry: Mechanically
852 Investigating Local Structure and Properties of Surfaces with the Atomic Force
853 Microscope. *J. Chem. Educ.* **2005**, *82* (5), 695–703. <https://doi.org/10.1021/ed082p695>.
- 854 (73) Heinz, W. F.; Hoh, J. H. Spatially Resolved Force Spectroscopy of Biological Surfaces
855 Using the Atomic Force Microscope. *Trends Biotechnol.* **1999**, *17* (4), 143–150.
856 [https://doi.org/10.1016/S0167-7799\(99\)01304-9](https://doi.org/10.1016/S0167-7799(99)01304-9).
- 857 (74) Ertz, D.; Löhmus, A.; Löhmus, R.; Olin, H.; Pokropivny, A. V.; Ryen, L.; Svensson, K.
858 Force Interactions and Adhesion of Gold Contacts Using a Combined Atomic Force
859 Microscope and Transmission Electron Microscope. *Appl. Surf. Sci.* **2002**, *188* (3–4),
860 460–466. [https://doi.org/https://doi.org/10.1016/S0169-4332\(01\)00933-3](https://doi.org/https://doi.org/10.1016/S0169-4332(01)00933-3).
- 861 (75) Thewes, N.; Loskill, P.; Jung, P.; Peisker, H.; Bischoff, M.; Herrmann, M.; Jacobs, K.
862 Hydrophobic Interaction Governs Unspecific Adhesion of Staphylococci: A Single Cell
863 Force Spectroscopy Study. *Beilstein J. Nanotechnol.* **2014**, *5*, 1501–1512.
864 <https://doi.org/10.3762/bjnano.5.163>.
- 865 (76) Butt, H.-J.; Cappella, B.; Kappl, M. Force Measurements with the Atomic Force
866 Microscope: Technique, Interpretation and Applications. *Surf. Sci. Rep.* **2005**, *59* (1), 1–
867 152. <https://doi.org/https://doi.org/10.1016/j.surfrep.2005.08.003>.
- 868 (77) Binahmed, S.; Hasane, A.; Wang, Z.; Mansurov, A.; Romero-Vargas Castrillón, S.
869 Bacterial Adhesion to Ultrafiltration Membranes: Role of Hydrophilicity, Natural Organic
870 Matter, and Cell-Surface Macromolecules. *Environ. Sci. Technol.* **2018**, *52* (1), 162–172.
871 <https://doi.org/10.1021/acs.est.7b03682>.
- 872 (78) Li, Q.; Pan, X.; Qu, Z.; Zhao, X.; Jin, Y.; Dai, H.; Yang, B.; Wang, X. Understanding the
873 Dependence of Contact Angles of Commercially RO Membranes on External Conditions

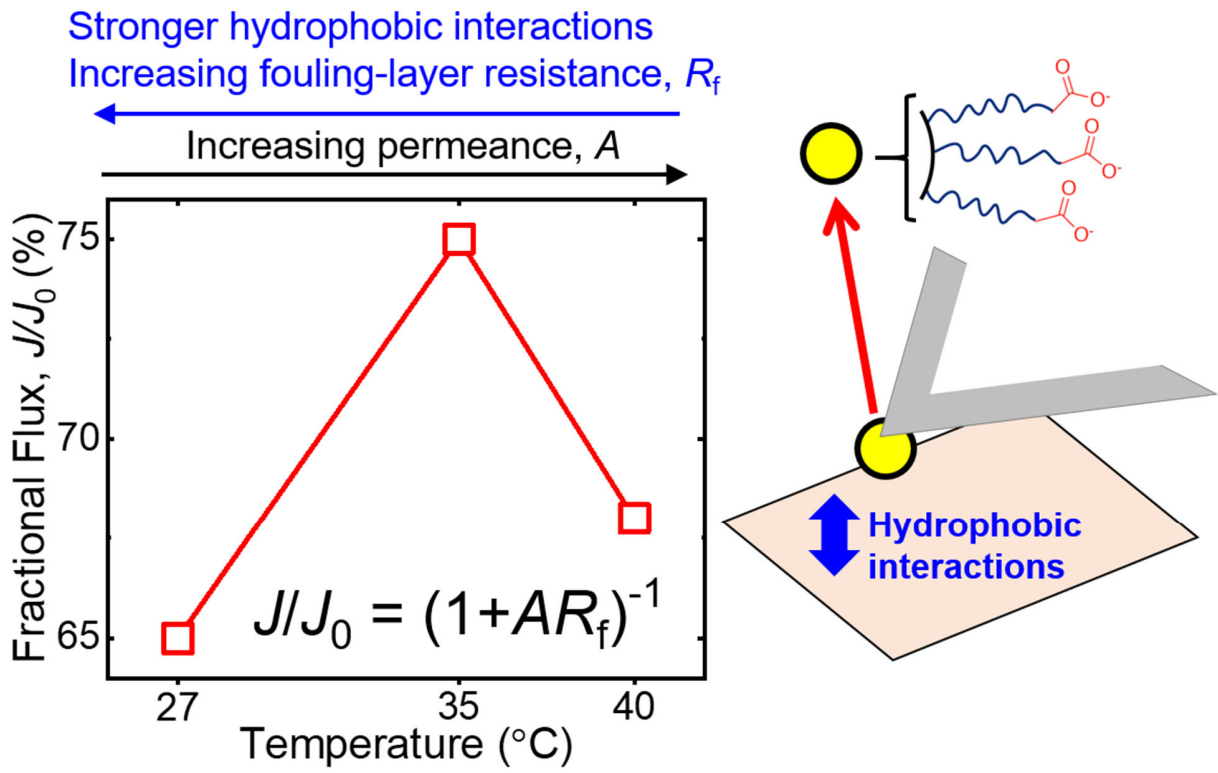
- 874 and Surface Features. *Desalination* **2013**, *309*, 38–45.
875 <https://doi.org/10.1016/j.desal.2012.09.007>.
- 876 (79) Akin, O.; Temelli, F. Probing the Hydrophobicity of Commercial Reverse Osmosis
877 Membranes Produced by Interfacial Polymerization Using Contact Angle, XPS, FTIR,
878 FE-SEM and AFM. *Desalination* **2011**, *278* (1–3), 387–396.
879 <https://doi.org/10.1016/j.desal.2011.05.053>.
- 880 (80) Miller, D. J.; Dreyer, D. R.; Bielawski, C. W.; Paul, D. R.; Freeman, B. D. Surface
881 Modification of Water Purification Membranes. *Angew. Chemie Int. Ed.* **2017**, *56* (17),
882 4662–4711. <https://doi.org/10.1002/anie.201601509>.
- 883 (81) Andrade, J. D.; Smith, L. M.; Gregonis, D. E. The Contact Angle and Interface Energetics.
884 In *Surface and Interfacial Aspects of Biomedical Polymers*; Springer US: Boston, MA,
885 1985; Vol. 1, pp 249–292. https://doi.org/10.1007/978-1-4684-8610-0_7.
- 886 (82) Surawanjijit, S.; Rahardianto, A.; Cohen, Y. An Integrated Approach for Characterization
887 of Polyamide Reverse Osmosis Membrane Degradation Due to Exposure to Free Chlorine.
888 *J. Memb. Sci.* **2016**, *510*, 164–173. <https://doi.org/10.1016/j.memsci.2016.02.044>.
- 889 (83) Diaz, M. E.; Savage, M. D.; Cerro, R. L. The Effect of Temperature on Contact Angles
890 and Wetting Transitions for N-Alkanes on PTFE. *J. Colloid Interface Sci.* **2017**, *503*, 159–
891 167. <https://doi.org/10.1016/j.jcis.2017.05.003>.
- 892 (84) Yang, J.; Lee, S.; Lee, E.; Lee, J.; Hong, S. Effect of Solution Chemistry on the Surface
893 Property of Reverse Osmosis Membranes under Seawater Conditions. *Desalination* **2009**,
894 *247* (1–3), 148–161. <https://doi.org/10.1016/j.desal.2008.12.020>.
- 895 (85) Tu, K. L.; Chivas, A. R.; Nghiem, L. D. Effects of Chemical Preservation on Flux and
896 Solute Rejection by Reverse Osmosis Membranes. *J. Memb. Sci.* **2014**, *472*, 202–209.
897 <https://doi.org/10.1016/j.memsci.2014.08.052>.
- 898 (86) Zisman, W. A. Relation of the Equilibrium Contact Angle to Liquid and Solid
899 Constitution. In *Contact Angle, Wettability, and Adhesion*; 1964; pp 1–51.
900 <https://doi.org/10.1021/ba-1964-0043.ch001>.
- 901 (87) Petke, D. F.; Ray, R. B. Temperature Dependence of Contact Angles of Liquids on
902 Polymeric Solids. *J. Colloid Interface Sci.* **1969**, *31* (2), 216–227.
- 903 (88) Nilsson, M.; Trägårdh, G.; Östergren, K. The Influence of PH, Salt and Temperature on
904 Nanofiltration Performance. *J. Memb. Sci.* **2008**, *312* (1–2), 97–106.
905 <https://doi.org/10.1016/j.memsci.2007.12.059>.
- 906 (89) Kasemset, S.; He, Z.; Miller, D. J.; Freeman, B. D.; Sharma, M. M. Effect of
907 Polydopamine Deposition Conditions on Polysulfone Ultrafiltration Membrane Properties
908 and Threshold Flux during Oil/Water Emulsion Filtration. *Polymer (Guildf)*. **2016**, *97*,
909 247–257. <https://doi.org/10.1016/j.polymer.2016.04.064>.
- 910 (90) Kudin, K. N.; Car, R. Why Are Water-Hydrophobic Interfaces Charged? *J. Am. Chem.*
911 *Soc.* **2008**, *130* (12), 3915–3919. <https://doi.org/10.1021/ja077205t>.
- 912 (91) Seo, Y.; Jhe, W. Atomic Force Microscopy and Spectroscopy. *Reports Prog. Phys.* **2008**,
913 *71* (1), 016101. <https://doi.org/10.1088/0034-4885/71/1/016101>.
- 914 (92) Thewes, N.; Thewes, A.; Loskill, P.; Peisker, H.; Bischoff, M.; Herrmann, M.; Santen, L.;
915 Jacobs, K. Stochastic Binding of Staphylococcus Aureus to Hydrophobic Surfaces. *Soft*
916 *Matter* **2015**, *11* (46), 8913–8919. <https://doi.org/10.1039/C5SM00963D>.
- 917 (93) Lee, S.; Elimelech, M. Relating Organic Fouling of Reverse Osmosis Membranes to
918 Intermolecular Adhesion Forces. *Environ. Sci. Technol.* **2006**, *40* (3), 980–987.
919 <https://doi.org/10.1021/es051825h>.

- 920 (94) Kocun, M.; Grandbois, M.; Cuccia, L. A. Single Molecule Atomic Force Microscopy and
921 Force Spectroscopy of Chitosan. *Colloids Surfaces B Biointerfaces* **2011**, *82* (2), 470–476.
922 <https://doi.org/10.1016/j.colsurfb.2010.10.004>.
- 923 (95) Stock, P.; Utzig, T.; Valtiner, M. Direct and Quantitative AFM Measurements of the
924 Concentration and Temperature Dependence of the Hydrophobic Force Law at
925 Nanoscopic Contacts. *J. Colloid Interface Sci.* **2015**, *446*, 244–251.
926 <https://doi.org/10.1016/j.jcis.2015.01.032>.
- 927 (96) Dallin, B. C.; Yeon, H.; Ostwalt, A. R.; Abbott, N. L.; Van Lehn, R. C. Molecular Order
928 Affects Interfacial Water Structure and Temperature-Dependent Hydrophobic Interactions
929 between Nonpolar Self-Assembled Monolayers. *Langmuir* **2019**, *35* (6), 2078–2088.
930 <https://doi.org/10.1021/acs.langmuir.8b03287>.
- 931 (97) Huang, D. M.; Chandler, D. Temperature and Length Scale Dependence of Hydrophobic
932 Effects and Their Possible Implications for Protein Folding. *Proc. Natl. Acad. Sci.* **2000**,
933 *97* (15), 8324–8327. <https://doi.org/10.1073/pnas.120176397>.
- 934 (98) Stillinger, F. H. Structure in Aqueous Solutions of Nonpolar Solutes from the Standpoint
935 of Scaled-Particle Theory. *J. Solution Chem.* **1973**, *2* (2–3), 141–158.
936 <https://doi.org/10.1007/BF00651970>.
- 937 (99) Huang, D. M.; Geissler, P. L.; Chandler, D. Scaling of Hydrophobic Solvation Free
938 Energies. *J. Phys. Chem. B* **2001**, *105* (28), 6704–6709.
939 <https://doi.org/10.1021/jp0104029>.
- 940 (100) Elimelech, M.; Childress, A. E. *Zeta Potential of Reverse Osmosis Membranes:
941 Implications for Membrane Performance*; 1996.
- 942 (101) Jermann, D.; Pronk, W.; Meylan, S.; Boller, M. Interplay of Different NOM Fouling
943 Mechanisms during Ultrafiltration for Drinking Water Production. *Water Res.* **2007**, *41*
944 (8), 1713–1722. <https://doi.org/10.1016/j.watres.2006.12.030>.
- 945 (102) Mehdizadeh, H.; Dickson, J. M.; Eriksson, P. K. Temperature Effects on the Performance
946 of Thin-Film Composite, Aromatic Polyamide Membranes. *Ind. Eng. Chem. Res.* **1989**, *28*
947 (6), 814–824. <https://doi.org/10.1021/ie00090a025>.
- 948 (103) Madaeni, S. S.; Mansourpanah, Y. Chemical Cleaning of Reverse Osmosis Membranes
949 Fouled by Whey. *Desalination* **2004**, *161* (1), 13–24.
950 [https://doi.org/https://doi.org/10.1016/S0011-9164\(04\)90036-7](https://doi.org/https://doi.org/10.1016/S0011-9164(04)90036-7).
- 951 (104) Karan, S.; Jiang, Z.; Livingston, A. G. Sub-10 Nm Polyamide Nanofilms with Ultrafast
952 Solvent Transport for Molecular Separation. *Science (80-.)*. **2015**, *348* (6241), 1347–
953 1351. <https://doi.org/10.1126/science.aaa5058>.
- 954 (105) Fujioka, T.; Oshima, N.; Suzuki, R.; Price, W. E.; Nghiem, L. D. Probing the Internal
955 Structure of Reverse Osmosis Membranes by Positron Annihilation Spectroscopy:
956 Gaining More Insight into the Transport of Water and Small Solutes. *Journal of
957 Membrane Science*. 2015, pp 106–118. <https://doi.org/10.1016/j.memsci.2015.02.007>.
- 958 (106) Goh, P. S.; Lau, W. J.; Othman, M. H. D.; Ismail, A. F. Membrane Fouling in
959 Desalination and Its Mitigation Strategies. *Desalination* **2018**, *425*, 130–155.
960 <https://doi.org/10.1016/j.desal.2017.10.018>.
- 961 (107) Liu, J.; Huang, T.; Ji, R.; Wang, Z.; Tang, C. Y.; Leckie, J. O. Stochastic Collision-
962 Attachment-Based Monte Carlo Simulation of Colloidal Fouling: Transition from Foulant-
963 Clean-Membrane Interaction to Foulant-Fouled-Membrane Interaction. *Environ. Sci.
964 Technol.* **2020**, *54* (19), 12703–12712. <https://doi.org/10.1021/acs.est.0c04165>.
- 965 (108) Henis, J. M. S.; Tripodi, M. K. Composite Hollow Fiber Membranes for Gas Separation:

- 966 The Resistance Model Approach. *J. Memb. Sci.* **1981**, 8 (3), 233–246.
967 [https://doi.org/10.1016/S0376-7388\(00\)82312-1](https://doi.org/10.1016/S0376-7388(00)82312-1).
- 968 (109) Sagle, A. C.; Van Wagner, E. M.; Ju, H.; McCloskey, B. D.; Freeman, B. D.; Sharma, M.
969 M. PEG-Coated Reverse Osmosis Membranes: Desalination Properties and Fouling
970 Resistance. *J. Memb. Sci.* **2009**. <https://doi.org/10.1016/j.memsci.2009.05.013>.
- 971 (110) Ang, W. S.; Tiraferri, A.; Chen, K. L.; Elimelech, M. Fouling and Cleaning of RO
972 Membranes Fouled by Mixtures of Organic Foulants Simulating Wastewater Effluent. *J.*
973 *Memb. Sci.* **2011**, 376 (1–2), 196–206. <https://doi.org/10.1016/j.memsci.2011.04.020>.
- 974 (111) Torres, M. L.; Fernandez, J. M.; Dellatorre, F. G.; Cortizo, A. M.; Oberti, T. G.
975 Purification of Alginate Improves Its Biocompatibility and Eliminates Cytotoxicity in
976 Matrix for Bone Tissue Engineering. *Algal Res.* **2019**, 40, 101499.
977 <https://doi.org/10.1016/j.algal.2019.101499>.

978
979
980
981
982
983
984
985
986
987
988

989



990

991

TOC Figure